Study on impurity screening in stochastic magnetic boundary of the Large Helical Device

M. Kobayashi 1), Y. Feng 2), S. Morita 1), M.B. Chowdhuri 1), S. Masuzaki 1), M. Goto 1), N. Ohyabu 1), T. Morisaki 1), H. Yamada 1), I. Yamada 1), K. Narihara 1), A. Komori 1), O. Motojima 1) and the LHD experimental group

1) National Institute for Fusion Science, Toki 509-5292, Japan
2) Max-Planck-Institute fuer Plasmaphysik, Wendelsteinstrasse 1, D-17491 Greifswald, Germany

e-mail contact of main author: kobayashi.masahiro@lhd.nifs.ac.jp

Abstract. The impurity transport characteristics in the scrape-off layer associated with a stochastic magnetic boundary of LHD are analyzed. The remnant islands with very small internal field line pitch in the stochastic region play a key role in reducing the impurity influx. The thermal force driven impurity influx is significantly suppressed when the perpendicular energy flux exceeds the parallel one inside the islands due to the small pitch. Application of the 3D edge transport code, EMC3-EIRENE, confirmed the impurity retention (screening) effect in the edge region. It is also found that the edge surface layers are the most effective region to retain (screen) impurities because of the flow acceleration and plasma cooling via short flux tubes. The carbon emission obtained in experiments is in good agreement with the modelling results, showing the impurity retention (screening) potential of the stochastic magnetic boundary.

1. Introduction

Understanding the impurity transport in magnetically confined fusion devices is one of the most important issues for realizing clean core plasmas as well as for control of edge cooling via impurity radiation. The impurities released at plasma facing components by physical/chemical sputtering first undergo the scrape-off layer (SOL) transport, which then determines influx into core plasma across the last closed flux surface (LCFS). Control of the edge plasma transport by stochastic magnetic field structure has been proposed, where an enhanced transport by the braiding magnetic field [1] was expected to improve impurity screening as well as to reduce peak power load at the plasma facing components. Experimental indications of core plasma decontamination associated with the edge stochastic field have, indeed, been observed [2-5]. The models of impurity screening to explain the phenomena have been developed as well [6,7], where the three dimensionality of the field line stochasticity is sensibly reduced into one dimensional model. There, however, still remain the following questions :

1. How does the "core" decontamination relate to the "edge" stochastic magnetic field structure?
2. To what extent do the reduced expressions of the stochastic field line effect agree with a three dimensional modelling that allows a realistic treatment of the complex field line structure?

3D modelling of the stochastic magnetic field is made possible by the edge transport code EMC3 [8] which has been developed for divertor transport analysis of stellarator W7-AS. The application of the code to W7-AS has shown a clear impurity retention (screening) effect of the island divertor at high density discharges [9], where the friction force dominates over the ion thermal force in the islands. This is the one of the candidates for explaining impurity screening mechanism at the HDH regime in W7-AS. The application of the code to the LHD edge stochastic SOL has also predicted an impurity retention (screening) effect of the edge region at high density operations [10]. In both W7-AS and LHD, the key role to suppress the thermal force is identified to be the perpendicular energy transport inside the (remnant) magnetic islands in the island divertor as well as in the stochastic magnetic boundary. In the latter case, the enhanced friction force in the edge surface layer with mixture of long and short flux tubes is found to provide an effective retention effect as well. The first direct comparison

between modellings and experiments has been carried out, where the calculated density dependence of carbon line emission through the stochastic boundary agrees qualitatively with those from carbon spectroscopic measurements [11]. In this paper, the SOL impurity transport characteristics in the stochastic magnetic boundary are discussed in analytical form in order to better understand the 3D modelling results as well as the experimental observations. The results of the 3D modelling with an improved impurity source treatment derived from experimental data are presented in comparison with carbon emission measurements.

2. Impact of flux tube geometry on SOL impurity transport

In the stochastic magnetic boundary, it is found that there exist remnant magnetic islands with substantial spatial size of an order of centimetres. Figure 1 shows the connection length (L_c, left half) and electron temperature (right half) distributions at the edge region of LHD, superposed with Poincare plots of field line trajectories. The radial coordinate r_{eff} is defined by a constant volume in cylindrical approximation enclosed by each radial computational mesh. The electron temperature (Te) is obtained by EMC3/EIRENE. The clear remnant islands of poloidal mode of m=8, 7, 6 ... are identified with the while colour of L_c which indicates the length more than 10^5 m. Since the heliotron magnetic configuration of LHD has ten toroidal field periods, the low order resonances appear at rotational transform of $\iota = 10/8$, 10/7, 10/6, respectively. The separatrix of the islands are not clear because of the island overlap each other. Higher order modes like the n/m=20/15, 20/13 ... are still visible in the Poincare plots but with strongly reduced size since the perturbation field strength decays radially as r^{m-1} with r being minor radius, i.e. the higher modes decays much quicker than the
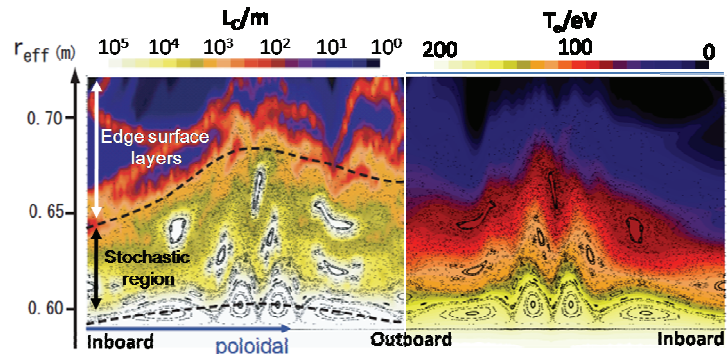

FIG. 1. Connection length (left half) and electron temperature (right half) distributions in the edge region of LHD, superposed with Poincare plot. The magnetic field structure in this plane is up-down symmetric around the "outboard" in this figure.
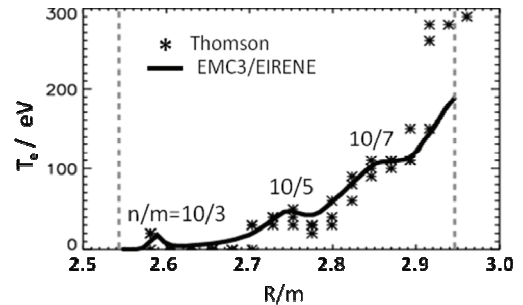

FIG. 2. Radial profiles of electron temperature obtained by Thomson scattering system (*) together with that by EMC3/EIRENE (solid line). The profile is the one at the midplane of inboard side.

lower ones. It is, therefore, difficult to realize a broad mode number spectrum to make the field line trajectories diffusive. Related numerical analysis in this respect can be found in ref.[12]. The essential message provided by this study is that the basic structure of the low order modes remain in spite of the perturbation from the higher-order resonances. The outer region outside the m=5 mode is distingushed from the inner region by the co-existance of flux tubes of short and long connection length. The region is called edge surface layers, while the inner region is called stochastic region [13].

The impact of the lower order islands on the background plasma transport (energy, particle and momentum) has been studied numerically [14,15]. The electron temperature distribution is modulated by the islands, as shown in figure 1 (right). This is confirmed by the electron temperature profile along the inboard side midplane, measured by the Thomson scattering system, which is shown in figure 2. Flattening of Te at m=7 and 5 modes is clearly identified. Recent probe measurements also show an indication of the plasma particle transport well aligned with the islands structure [16].

Such the effect of the islands plays a significant role on the parameter dependence of the impurity transport characteristics. The leading terms in parallel impurity transport momentum equation are considered to be the friction force and the force that originates from ion temperature gradient (called "thermal force"). The friction force is expressed as, $m_z \dfrac{V_{i//} - V_{z//}}{\tau_{zi}}$, where $m_z, V_{z//}, V_{i//}, \tau_{zi}$ are mass of impurity, parallel velocity of impurity and background ion, and the slowing down time of impurity colliding with background ions, respectively. The "thermal force" originates from the collision between the impurity and the background ions that comes from cooler and hotter region due to the parallel temperature gradient. This then creates imbalance of momentum transfer due to the dependence of $\tau_{zi} \propto T_i^{1.5}$. The fluid expression reads, $C_i \dfrac{\partial T_i}{\partial s}$,

where s represent coordinate along field lines that directs towards divertor plates, and C_i is the numerical factor, $2.6Z^2$, when $m_i \ll m_z$. In spite of the collisional nature of the force, the collision time does not appear in the form due to the cancellation at substantial collisionality [17]. Since the background plasma flows towards divertor plates, the friction force push the impurity
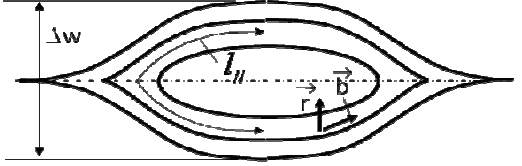

FIG. 3. Schematic picture of remnant island and the notations of $\Delta w, l_{//}, \vec{r}, \vec{b}$. Although the separatrix is vague in Poincare plot in figure 1, the plasma feels the structure of islands. The figure represents the separatrix seen by plasma transport on average.

to downstream (divertor), on the other hand, because of the parallel temperature gradient which directs to upstream, the thermal force drives impurity to upstream (LCFS). In steady state with the two terms being balanced, the parallel impurity velocity is determined by,

$$V_{z//} \approx V_{i//} + C_i \frac{\tau_{zi}}{m_z} \frac{\partial T_i}{\partial s} = V_{i//}(1 - \alpha), \qquad (1)$$

with,

$$\alpha = \frac{thermal\ force}{friction\ force} = \frac{C_i C_\tau}{C_V m_z} \frac{T_i \left| \partial T_i / \partial s \right|}{M\ n_i}, \qquad (2)$$

where M is Mach number, and C_τ and C_V are numerical constants defined as $\tau_{zi} = C_\tau T_i^{1.5} / n_i$ and $V_{i//} = C_V M T_i^{0.5}$, respectively. The sign of $V_{z//}$ is determined by the magnitude of α. Impurity retention (screening) is defined by $V_{z//} > 0$ with $\alpha < 1$.

As shown above, because of remnant islands in stochastic magnetic region, the radial conductive energy flux consists of perpendicular and parallel ones,

$$q_{r,cond} = f_{cond} \times q_{r,total} = -n\chi_\perp \frac{\partial T_i}{\partial r} - \kappa_{i0} T_i^{2.5} \frac{\partial T_i}{\partial s} \vec{b} \cdot \vec{r}, \quad (3)$$

where $\vec{b}, \vec{r}$ are local base vectors tangential to field line and in radial direction, respectively (figure 3). f_{cond} is a fraction of conductive energy out of total flux. The first term represents energy flux in perpendicular direction (r), and the second term is projection of parallel energy flux onto radial direction due to the stochastic magnetic field. Using $\dfrac{\partial}{\partial s} = \vec{b} \cdot \vec{r} \dfrac{\partial}{\partial r}$,

the parallel temperature gradient becomes,

$$\frac{\partial T_i}{\partial s} = -\frac{q_{r,total}\ f_{cond}\ \Theta}{n\chi_\perp + \kappa_{i0} T_i^{2.5} \Theta^2}, \qquad (4)$$

with $\Theta = \vec{b} \cdot \vec{r}$ which corresponds to internal field line pitch inside the islands. The condition that the perpendicular energy flux (the first term in denominator) dominates over the parallel one (the second term) is [9], $\frac{n\chi_\perp}{\kappa_{i0}T_i^{2.5}} >> \Theta^2$. The internal pitch on average inside islands can be approximated as $\Theta \sim \frac{\Delta w}{l_{//}}$, where $\Delta w, l_{//}$ are island width and distance along field line to circumference inside island (figure 3). This can be also written as $\Theta = \frac{\Delta w^2 m}{4\pi R}\iota' \approx \frac{4B_r}{\pi B_\phi}$, where $m, R, \iota', B_r, B_\phi$ are poloidal mode number of island, major radius, magnetic shear, $d\iota/dr$, radial and toroidal magnetic field strength, respectively. In the LHD edge region, this is estimated to be $\sim 10^{-4}$ with R=3.75 m, m~7, Δw~0.01 m and ι'~8 m^{-1}. For typical edge parameters, n=10^{19} m^{-3} and T$_i$=100eV, the right hand side becomes $\frac{n\chi_\perp}{\kappa_{i0}T_i^{2.5}}$~$10^{-7}$, while Θ^2~10^{-8}. The perpendicular energy transport across the islands thus dominates over parallel one, in which case the temperature gradient is expressed as,

$$\frac{\partial T_i}{\partial s} \approx -\frac{q_{r,total}\, f_{cond}\,\Theta}{n\chi_\perp}. \qquad (5)$$

The parallel temperature gradient is inversely proportional to the density. Substituting this expression into eq.(2), one gets,

$$\alpha = \frac{thermal\ force}{friction\ force} = \frac{C_i C_\tau}{C_V m_z}\frac{\Theta\, q_{r,total}\, f_{cond}\, T_i}{\chi_\perp M\, n_i^2}. \qquad (6a)$$

There appears rather strong dependence on density. Increase of the density generally leads to reduction of temperature with fixed input power. Actually, in the previous study, density dependence is observed as $T \propto n^{-0.5\sim-1}$ in the entire edge region of LHD [14,18]. The relatively moderate dependence is because of the perpendicular loss of momentum caused by the island structure, which breaks pressure conservation along flux tubes. Provided that the other parameters, $f_{cond}, \chi_\perp, M$, are not very sensitive to the density,

$$\alpha = \frac{thermal\ force}{friction\ force} \propto \frac{q_{r,total}\, f_{cond}}{\chi_\perp M\, n_i^{2.5\sim3}} \propto n^{-2.5\sim-3}. \qquad (6b)$$

The thermal force is strongly reduced by increasing density in the stochastic SOL.

The eq.(6a) has also the dependence of $\alpha \propto f_{cond}/M$, meaning that acceleration of plasma flow is effective to increase the friction force by increasing M and reducing f_{cond} simultaneously. This usually happens near divertor plates. As shown later, the effect becomes remarkable in the edge surface layer of the stochastic boundary with enhanced acceleration by short flux tubes which act as target-equivalent sink. Although the resulting impurity distribution in the SOL is determined by an overall effect of parallel and perpendicular transport as well as neutral impurity penetration length, the strong density dependence of eq.(6b) indicates a possibility to obtain an impurity retention in the stochastic magnetic boundary plasma with increasing density, which is caused by the flux tube geometry of the remnant islands.

3. Three dimensional modelling of Impurity transport in stochastic magnetic boundary
3.1 Model
3D impurity transport modelling in the stochastic magnetic boundary of LHD has been carried out using EMC3 [8] which is coupled with EIRENE [19]. The EMC3 solves the

conservation form of Braginskii equations of mass, momentum and energy for electrons and ions with Monte Carlo scheme, in realistic three dimensional geometry of magnetic fields and divertor plates as well as first wall. Recycling neutrals are released at the divertor plates weighted with particle deposition distribution and traced kinetically by EIRENE. The computation domain covers the entire edge region of LHD, that starts from the LCFS and ends at the edge of the stochastic boundary close to the divertor plates. The boundary conditions at the LCFS is input power into the SOL, P_{SOL}, which is estimated from power deposition calculations for neutral beam injection (NBI) in experiments, and fixed density at the LCFS (n_{LCFS}) which is fit to the density obtained by the microwave interferometer. In the present analysis, it is found that n_{LCFS} is nearly equal to the line averaged density. The boundary condition at the downstream is the Bohm condition for energy and particle flux to the divertor plates. The transport coefficients perpendicular to magnetic fields are assumed to be anomalous ones and spatially constant. The coefficients are adjusted to fit the temperature and density profiles obtained by Thomson scattering system. The measured profiles are well reproduced by simulations for discharges of different densities. The coefficients are found to be less sensitive to the density scan. For the impurity transport, the parallel momentum balance equation [20] is solved with assumption of $T_z = T_i$. The mass conservation is treated as,

$$\vec{\nabla} \cdot \left(n_z V_{z//} \vec{b} - D_z \vec{b}_\perp \vec{b}_\perp \cdot \vec{\nabla} n_z \right) = S_{z-1 \to z} n_{z-1} - S_{z \to z+1} n_z + R_{z+1 \to z} n_{z+1} - R_{z \to z-1} n_z , \qquad (7)$$

where D_z, S, R are diffusion coefficient of impurities, ionization and recombination rate, respectively. $\vec{b}_\perp$ is defined as $\vec{b}_\perp \vec{b}_\perp = \vec{I} - \vec{b}\vec{b}$ with $\vec{I}$ being a unit tensor. The parallel electric field in the momentum equation is obtained by momentum equation of electrons [8]. D_z is set to the same value as that of background plasma particle diffusivity, i.e. $D_z = D = 0.5$ m^2/s obtained from the fitting procedure described above.

In the present analysis, the impurity species is carbon which is produced at the graphite divertor plates via either physical or chemical sputtering process. In addition, the first wall is also a candidate for source origin because of the carbon deposition layers observed [21]. Using the probe measurements at the divertor plate as well as the calculated charge exchange neutral flux to the first wall from EIRENE, the physical sputtering coefficients are estimated from the Bohdansky's formula [22]. The ejection energy spectra of the carbon were estimated using Falcone's [23] and Kenmotsu's [24] formulae, both giving peaks around 2eV for divertor and first wall sputtering. The chemical sputtering has large uncertainty. There exists dependences on wall temperature and the bombarding flux, as reported in ref.[25] and weak dependence on the bombarding energy. The temperature of the divertor plates and the first wall during discharges are almost constant at ~ 200 and 40 ^{o}C, respectively. The fluxes to the divertors and first wall are ~10^{23} and ~10^{21} m^{-2}s^{-1}, respectively. Chemical sputtering, in comparison to physical one, is characterized by the features of the low ejection energy of sputtered atoms and the weak dependence on energy of bombarding particles. This will result in a linearly increasing sputtering yield with increasing divertor/first wall flux. For simplicity, the chemical sputtering coefficient is set to 0.01 for the present analysis. The resulting sputtering yields are plotted in figure 4. Clear difference between the physical and chemical sputtering yields is seen: The physical sputtering yields increase slightly with density rise and soon saturate around 3×10^{19} m^{-3} due to the decreasing bombardment energy, while the chemical
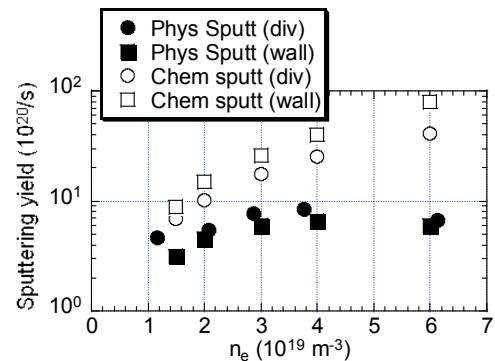
FIG. 4.Sputtering yield estimated for the divertor plates and the first wall. The closed and open symbols are for physical and chemical sputtering, respectively. The circles and squares are for divertor and first wall, respectively.

ones constantly increase with the increasing density. The physical sputtering process is comparable to that of chemical one only at low densities. The chemical sputtering process becomes dominant at high densities. From these results, the physical sputtering yield is assumed to be constant at 6×10^{20} s^{-1} for both of divertor plates and the first wall in the modelling. The source distribution on the targets is proportional to the particle deposition, while a uniform carbon source is assumed at the first wall. The ejection energies of carbon atoms are set to be 2eV and 0.05eV for the physical and chemical sputtering, respectively. It is found that the selection of the source in this way reproduces well the behavior of the measured CIII emission (from C^{2+}) (figure 7), which is considered to well reflect the source effect.

3.2 Results and comparison with experiments

Figure 5 shows the radial profiles of eq.(2) for different background plasma densities. At the low densities, the entire region is dominated by the ion thermal force which directs to upstream, while at the highest density the friction force dominates in almost the entire region. This is caused by the suppression of thermal force in the stochastic magnetic field structure discussed in the section 2. During the density scan, P_{SOL} was varied from 4MW to 8MW with increasing density. Taking into account the change of the power, the reduction of the ratio roughly

FIG. 5. Radial profiles of the ratio of thermal force to friction force, eq.(2), for different background densities. P_{SOL} is varied from 4MW to 8MW with increasing density.

follows the density dependences of eq.(6b). In addition, the sudden decrease of the ratio at around r_{eff} =0.67 m is attributed to the enhanced friction force at the edge surface layers where the plasma flow is effectively accelerated due to the short flux tubes which act as a target-relevant sink for particle and energy. The calculated carbon density profiles in the edge region are plotted in figure 6 for different background plasma densities and source locations of (a) physical sputtering from the divertor and (b) chemical sputtering from the first wall, respectively. At the lowest density, there appears large negative gradient of carbon density in the stochastic region, which is caused by the strong inward flow induced by the ion thermal force. In this case, substantial amount of carbon penetrates deeply inner than r_{eff} =0.68 m. As moving to the inner radius, the profiles become flat in spite of the large thermal force contribution as seen in figure 5. This is because of the decreasing Θ at the inner radius (note

that $\Theta \approx \dfrac{4B_r}{\pi B_\phi}$ and $B_r \propto r^{m-1}$), which then reduces radial component of the impurity flow,

i.e. $V_{zr} = \Theta V_{z//}$. With increasing density, the carbon density around the LCFS gradually decreases and the profiles through the stochastic region becomes flat, indicating no net inward flow of impurity. This is caused by the significant suppression of the thermal force in the stochastic magnetic structure as shown in figure 5. In addition, higher densities decrease the carbon penetration length so that the background plasma flows existing mainly in the edge surface layers can effectively push the impurities outwards by means of friction. This is clearly shown by the positive gradient of carbon profile around r_{eff} =0.68 m at n_{LCFS}=6.0x10^{19} m^{-3}. The case of the first wall physical sputtering results in deeper carbon penetration because of the thin stochastic region in front of the first wall. But the reduction of the carbon density at LCFS is observed as well similarly to figure 6 (a). The case of chemical
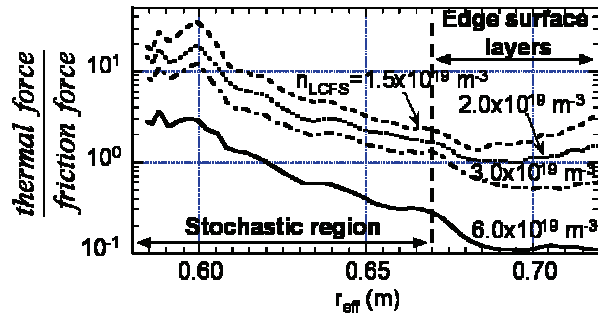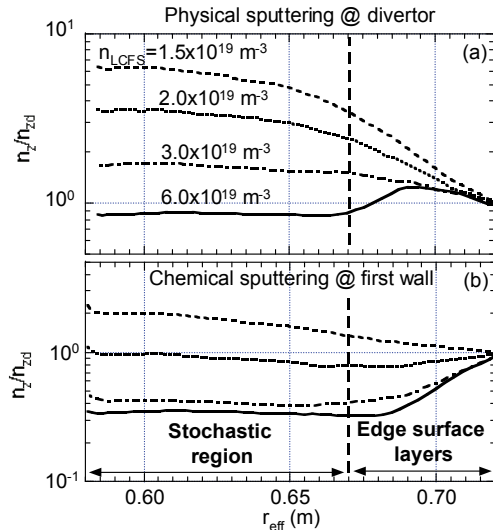
FIG. 6. Radial profiles of Carbon density summed over all charge states, normalized at the downstream density at r_{eff}=0.72 m. (a) physical sputtering from the divertor, (b) chemical sputtering from the first wall, respectively

sputtering from the first wall is plotted in figure 6 (b). In this case, the neutral carbon particles are ionized at the very edge of the stochastic boundary due to the low ejection energy, where the friction force is most effective to retain impurity caused by the flow acceleration in the edge surface layers. A clear screening is observed already at n_{LCFS}=2.0x10^{19} m^{-3}. For the low-energetic chemically-sputtered carbon atoms, the resulting carbon density profiles are rather insensitive to the source location. A divertor source gave similar results to those shown in figure 6 (b) for the wall-release case. In the all cases, it is found that the carbon density at the LCFS is significantly reduced at high densities.

The numerical results are compared with carbon emission measurements, which should reflect the change of carbon density profiles at the edge as obtained above. The carbon line radiation is measured with VUV monochromators and EUV spectrometer [26,27]. The selected lines and the corresponding charge states are CIII (C^{2+}) 977.020Å, CIV (C^{3+}) 1548.19Å, CV (C^{4+}) 40.268Å. The viewing area of the spectroscopy covers almost the entire region of the stochastic boundary. The measured emission intensity is plotted in figure 7 (a) as a function of density. The code results are shown in figure 7 (b) calculated using the same viewing geometry and taking into account both the physical and chemical sputtering processes as well as the source position effect. There are clear differences in density dependences between different charge states. The emission from the higher charge state, CV, strongly decreases with increasing density, while the emission from the lower charge states, CIV and CIII, increases slightly. It is noted that there is a large gap in ionization potential between CIV (64.5 eV) and CV (392 eV), which results in a clear spatial separation of the density profiles of these two charge states. The reduction of the carbon density around the LCFS by the suppression of the thermal force affects mostly the higher charge state, i.e. CV emission. It is also found that the large intensity of CV at the low densities is mainly due to the physically-sputtered high energetic carbon that can penetrate deeper in the stochastic region. On the other hand, the increase of the carbon at the very edge of the stochastic boundary contributes the increase of the lower charge states. This is clearly observed in the results of the modelling, which qualitatively agrees well with the experimental results.
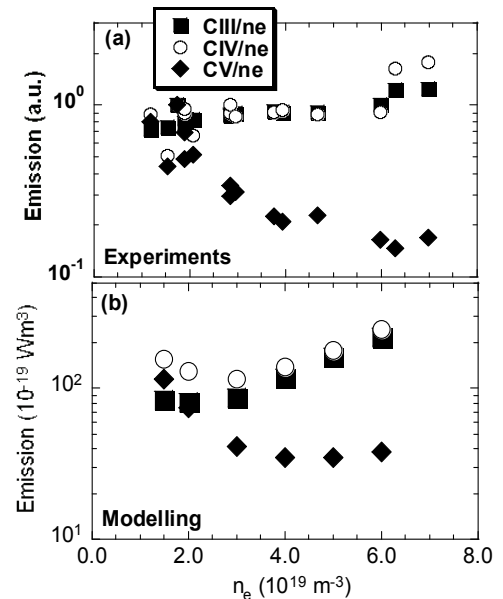

FIG. 7. Density dependence of carbon emission of CIII, CIV and CV. (a) experiments, (b) modelling. The emission of experiments is normalized by the values at the low density.

4. Summary

The impurity transport characteristics in the stochastic magnetic boundary of LHD are investigated. A force balance analysis shows that the remnant islands have an impurity

retention (screening) potential when the perpendicular energy transport dominates over the parallel one at high SOL densities. This is possible in LHD because of the small field line pitch (Θ) inside the islands. In this case, the ratio of the thermal force to friction force decreases with the density as $\dfrac{thermal\ force}{friction\ force} \propto n^{-2.5\sim-3}$. The 3D edge code EMC3-EIRENE shows that the strong suppression of the thermal force results in a significant reduction of the impurity density at the LCFS, insensitive to the source location and the ejection energy of impurity. The screening is most effective at the edge surface layers where the most of ionization of the neutral impurity takes place and the enhanced background plasma flow exists. The edge carbon emission from spectroscopic measurements agrees well with the modelling results, demonstrating the impurity screening potential of the stochastic magnetic boundary in LHD at high densities.

References
[1]   RECHESTER, A.B. and ROSENBLUTH, M.N., Phys. Rev. Lett. **40** (1978) 38.
[2]   GHENDRIH, Ph., GROSMAN, A. and CAPES, H., Plasma Phys. Control. Fusion **38** (1996) 1653.
[3]   CORRE, Y. et al., Nucl. Fusion **47** (2007) 119.
[4]   KOMORI, A. et al., J. Nucl. Mater. **313-316** (2003) 1267.
[5]   NAKAMURA, Y. et al., Nucl. Fusion **43** (2003) 219.
[6]   MOROZOV, D.Kh. et al., Phys. Plasmas **2** (1995) 1540.
[7]   TOKAR, M.Z., Phys. Plasmas **6** (1999) 2808.
[8]   FENG, Y. et al., Contrib. Plasma Phys. **44** (2004) 57.
[9]   FENG, Y. et al., Nucl. Fusion **46** (2006) 807.
[10] KOBAYASHI, M. et al., Contrib. Plasma Phys. **48** (2008) 255.
[11] KOBAYASHI, M. et al., "Model prediction of impurity retention in stochastic magnetic boundary and comparison with edge carbon emission in LHD", submitted to J. Nucl. Mater.
[12] DUECHS, D.F. et al., Plasma Phys. Control. Fusion **33** (1991) 919.
[13] OHYABU, N. et al., Nucl. Fusion **34** (1994) 387.
[14] KOBAYASHI, M. et al., J. Nucl. Mater. **363-365** (2007) 294.
[15] FENG, Y. et al., Nucl. Fusion **48** (2008) 024012.
[16] EZUMI, N., et al. "Plasma flow in the LHD ergodic layer", submitted to Plasma and Fusion Research.
[17] BRAGINSKII, S.I., in Review of Plasma Physics, edited by M. Leontovich (Consultants Bureau, New York, 1963), Vol. 1, p.205.
[18] MASUZAKI, S., et al., J. Nucl. Mater. **313-316** (2003) 852.
[19] REITER, D. et al., Fusion Sci. Technol. **47** (2005) 172.
[20] STANGEBY, P.C., and ELDER, J.D., Nucl. Fusion **35** (1995) 1391.
[21] HINO, T., et al., J. Nucl. Mater. **313-316** (2003) 167.
[22] BOHDANSKY, J., Nucl. Instrum. Methods B **2**, (1984) 587.
[23] FALCONE, G., Surface Science **187** (1987) 212.
[24] KENMOTSU, T., et al., J. Plasma Fusion Res. **80** (2004) 406.
[25] ROTH, J. et al., Nucl. Fusion **44** (2004) L21.
[26] CHOWDHURI, M.B., MORITA, S. and GOTO, M., et al., Rev. Sci. Instrum. **78** (2007) 023501.
[27] CHOWDHURI, M.B., MORITA, S. and GOTO, M., et al., Appl. Optics **47** (2008) 135.